Near Surface Geophysics

EAGE EUROPEAN ASSOCIATION OF GEOSCIENTISTS & ENGINEERS

Near Surface Geophysics, 2019, **17**, 487–499 doi: 10.1002/nsg.12060

Rayleigh-wave dispersion analysis using complex-vector seismic data

Xinming Qiu[1], Yun Wang[1]* and Chao Wang[2]

[1]*School of Geophysics and Information Technology, China University of Geosciences (Beijing), Beijing 100083, China, and* [2]*The State Key Laboratory of Ore Deposit Geochemistry, Institute of Geochemistry Chinese Academy of Sciences, Guiyang 550081, China*

Received March 2019, revision accepted July 2019

ABSTRACT

Identification of different modes of Rayleigh waves is essential in surface-wave surveys. Multi-mode Rayleigh waves can provide higher accuracy of the near-surface structure than the fundamental mode alone. However, some modes or frequencies of Rayleigh waves may be absent in the vertical-component seismic data. To complement the dispersion information, a method based on complex-vector seismic data is proposed. We construct the complex vector by setting the radial component and vertical component as the real part and imaginary part, respectively. Then, high-resolution linear Radon transform is used to obtain the multi-mode Rayleigh-wave dispersion image of the complex-vector seismic data. Based on different dispersion characteristics of the radial and vertical components, the dispersion images of the complex–vector seismic data show better performance against interferences and mode misidentification. Synthetic and field examples demonstrate advantages of the complex-vector method over the traditional vertical-component method in spectral bands and dispersion curve mode identification. Therefore, a more robust and accurate near-surface S-wave velocity structure can be expected compared to the traditional vertical-component Rayleigh-wave method.

Key words: Surface wave, Near-surface, S-wave velocity.

INTRODUCTION

Near-surface shear (S-) wave velocity is an important parameter in engineering and shallow seismic exploration. It is often used to evaluate the stiffness properties of near-surface media (e.g., Ivanov *et al.* 2010). S-wave velocity can be estimated using Rayleigh waves, because the phase velocity of Rayleigh wave is dominantly influenced by S-wave velocity (e.g., Xia, Miller and Park 1999). It is well known that Rayleigh wave is characterized by dispersion and have multiple modes in a layered near-surface model (e.g., Dal Moro 2014). Joint inversion of multi-mode Rayleigh waves attracts widespread interest due to less ambiguity and higher accuracy in S-wave velocity estimation (e.g., Xia *et al.* 2003; Song *et al.* 2007). In ambient noise tomography, the higher modes are used to examine azimuthal anisotropy in the lower crust and upper mantle (e.g., Harmon, Forsyth and Webb 2007). Joint inversion of different modes can constrain the crustal and upper mantle S-wave structure well (e.g., Yao *et al.* 2011).

In surface-wave surveys, multi-channel analysis of surface waves (MASW) is one of the most important methods, where the extracted dispersion curves are called experimental dispersion curves (e.g., Lu, Wang and Zhang 2007). Experimental dispersion curves may not correspond to one single mode but display as a superposition effect of different modes, because various modes of Rayleigh waves are recorded in seismic data (e.g., Lu *et al.* 2007; Lai, Mangriotis and Rix 2014). Of which, mode jumping is a common phenomenon where experimental dispersion curves rapidly alternate with different orders of modes. It may not only result in misidentification of Rayleigh-wave modes (Zhang and Chan 2003), but also produce incorrect velocity structures in shallow layers, especially when the vertical component is used alone and the near-surface model embed a low S-wave velocity layer (Mi *et al.* 2018).

*E-mail: wangyun@mail.gyig.ac.cn

Corresponding to the experimental dispersion curves, the apparent phase velocity, which comes from interference among multiple modes, is usually used to study the multi-mode superposition of Rayleigh waves (e.g., Tokimatsu, Tamura and Kojima 1992; Lai *et al.* 2014; Vaziri Astaneh and Guddati 2016). Previous studies on mode jumping and multi-mode superposition effects focused on the vertical component (e.g., Lu *et al.* 2007; Xia *et al.* 2012; Mi *et al.* 2018). It is important to develop studies on mode jumping for multi-component Rayleigh waves.

Rayleigh waves are traditionally acquired by a multi-channel vertical-component linear array and are activated by a hammer vertically impacting on a fixture (Olafsdottir, Bessason and Erlingsson 2018). High-resolution linear Radon transform (HLRT) is used to extract its dispersion curves (Luo *et al.* 2008). However, the experimental dispersion curves extracted from the vertical component have several defects, such as inaccurate phase velocities, mode misidentification and insufficient bandwidths (Boaga *et al.* 2013; Ikeda *et al.* 2015). These defects may affect accuracy and resolution of the S-wave velocity structure.

Rayleigh waves move elliptically along a radial plane in isotropic horizontal-layer media (Dal Moro 2014). Therefore, they can be recorded by both radial- and vertical-component geophones, in which the dispersive energy of Rayleigh waves show different distribution (Dal Moro and Ferigo 2011; Dal Moro, Moura and Moustafa 2015; Dal Moro, Moustafa and Al-Arifi 2018). When using the radial and vertical components jointly, Boaga *et al.* (2013) have verified that the mode misidentification can be overcome. Ikeda *et al.* (2015) ever used the dispersion image of the radial component to complement the vertical component. Pan *et al.* (2018) proposed stacking dispersive images from different components. However, the stacked dispersion image sometimes becomes worse when one of the components is polluted by strong interferences. So it is necessary to develop new methods to explore multi-component data.

In this work, we extend the studies on mode jumping for both radial and vertical components as well as explain the cause of mode jumping. In addition, we develop a complex-vector method to jointly use the radial and vertical components. First, the displacement and apparent phase velocities of the radial and vertical components are calculated to display their theoretical differences. Then, the energy distributions of Rayleigh waves in the radial and vertical components are compared. At last, the proposed method is tested by synthetic and field data to illustrate its advantages over the traditional vertical-component method.

DISPERSION CHARACTERISTICS OF MULTICOMPONENT RAYLEIGH WAVES

Displacement characteristics of multi-mode Rayleigh waves in the radial and vertical components

For a vertical point source, the theoretical ellipticity and vertical amplitude response of Rayleigh waves are respectively calculated using (Ikeda and Matsuoka 2013)

$$\frac{u_r}{u_z} = -\frac{Y_{12}}{Y_{14}}, \tag{1}$$

and

$$A_z = -\frac{k^2}{c} Y_{14} \left(\frac{\partial Y_{24}}{\partial c} \right)^{-1}, \tag{2}$$

where $Y_{14} = R_{12}R_{23} - R_{13}R_{22}$, $Y_{12} = R_{11}R_{23} - R_{13}R_{21}$, $Y_{24} = R_{12}R_{33} - R_{13}R_{32}$, c is the phase velocity of the Rayleigh wave, k is the wave number, A_z is the vertical amplitude response, u_r is the radial displacement and u_z is the vertical displacement. $R_{lm}(l,m = 1, 2, 3, 4)$ is the element of matrix **R**, as shown in the Appendix. Owing to the amplitude response proportional to the displacement, we obtain

$$\frac{A_r}{A_z} = -\frac{Y_{12}}{Y_{14}}. \tag{3}$$

By substituting equation (2) into equation (3), we obtain the radial amplitude response of Rayleigh waves

$$A_r = \frac{k^2}{c} Y_{12} \left(\frac{\partial Y_{24}}{\partial c} \right)^{-1}. \tag{4}$$

Lai *et al.* (2014) derived the analytical solutions for the apparent phase velocities of Rayleigh waves in the radial and vertical components, known as

$$V_r(r, z, \omega) = \frac{2\omega \sum_i \sum_j \left\{ \dfrac{w_1(z,k_i)w_1(z,k_j)w_2(z_s,k_i)w_2(z_s,k_j)\cos\left[r\left(k_i - k_j\right)\right]}{\left(c_i U_i I_i\right)\left(c_j U_j I_j\right)\sqrt{k_i k_j}} \right\}}{\sum_i \sum_j \left\{ \dfrac{w_1(z,k_i)w_1(z,k_j)w_2(z_s,k_i)w_2(z_s,k_j)\left(k_i + k_j\right)\cos\left[r\left(k_i - k_j\right)\right]}{\left(c_i U_i I_i\right)\left(c_j U_j I_j\right)\sqrt{k_i k_j}} \right\}}, \tag{5}$$

and

$$V_z(r, z, \omega) = \frac{2\omega \sum_i \sum_j \left\{ \dfrac{w_2(z,k_i)w_2(z,k_j)w_2(z_s,k_i)w_2(z_s,k_j)\cos\left[r\left(k_i - k_j\right)\right]}{\left(c_i U_i I_i\right)\left(c_j U_j I_j\right)\sqrt{k_i k_j}} \right\}}{\sum_i \sum_j \left\{ \dfrac{w_2(z,k_i)w_2(z,k_j)w_2(z_s,k_i)w_2(z_s,k_j)\left(k_i + k_j\right)\cos\left[r\left(k_i - k_j\right)\right]}{\left(c_i U_i I_i\right)\left(c_j U_j I_j\right)\sqrt{k_i k_j}} \right\}}, \tag{6}$$

Table 1 Parameters of Model 1

Thickness (m)	V_p (m/s)	V_s (m/s)	Density (kg/m^3)
1	200	100	2000
1	550	250	2000
3	1100	500	2000
5	1400	700	2000
40	2400	1400	2000
Infinite	3250	2000	2000

where w_1 and w_2 are the displacement eigenfunctions (Aki and Richards 2002). In fact, w_1 and w_2 are functions of the depth, wavenumber and frequency, that is $w_1 = w_1(z, k, \omega)$ and $w_2 = w_2(z, k, \omega)$. The frequency variable is omitted in the eigenfunctions to shorten equations (5) and (6). i or j is the mode order of Rayleigh waves, U is the group velocity, and I is the first energy integral of Rayleigh waves (Aki and Richards 2002; Lai *et al.* 2014). r is the offset, z is the depth of the receiver and z_s is the depth of the source. These equations make it easy to study the multi-mode effects on the experimental dispersion curves of Rayleigh waves.

A synthetic example is given to show the multi-mode effects on apparent phase velocities. For the layered model (Model 1 shown in Table 1), the ellipticity $|u_r/u_z|$, radial amplitude response $|A_r|/\sqrt{k}$ and vertical amplitude response $|A_z|/\sqrt{k}$ are, respectively, calculated using equations (1), (4) and (2), as shown in Fig. 1. Figure 1 also shows the apparent phase velocities of the Rayleigh waves in the radial and vertical component and the theoretical dispersion curves. Two main characteristics of multi-mode Rayleigh waves can be observed: (1) The ellipticity of all modes is changed with frequency. In addition, the first higher mode has different polarization characteristics from the fundamental mode, as shown in Fig. 1(a). (2) The radial amplitude response is greatly different from the vertical amplitude response, which causes their different apparent phase velocities. It can be found that the radial-component apparent phase velocities match well with the fundamental-mode dispersion curves at frequencies of 25–37 Hz, because the amplitude response of the fundamental mode is dominant in the radial component at those frequencies, as shown in Fig. 1(b). In contrast, vertical-component apparent phase velocities are between the theoretical phase

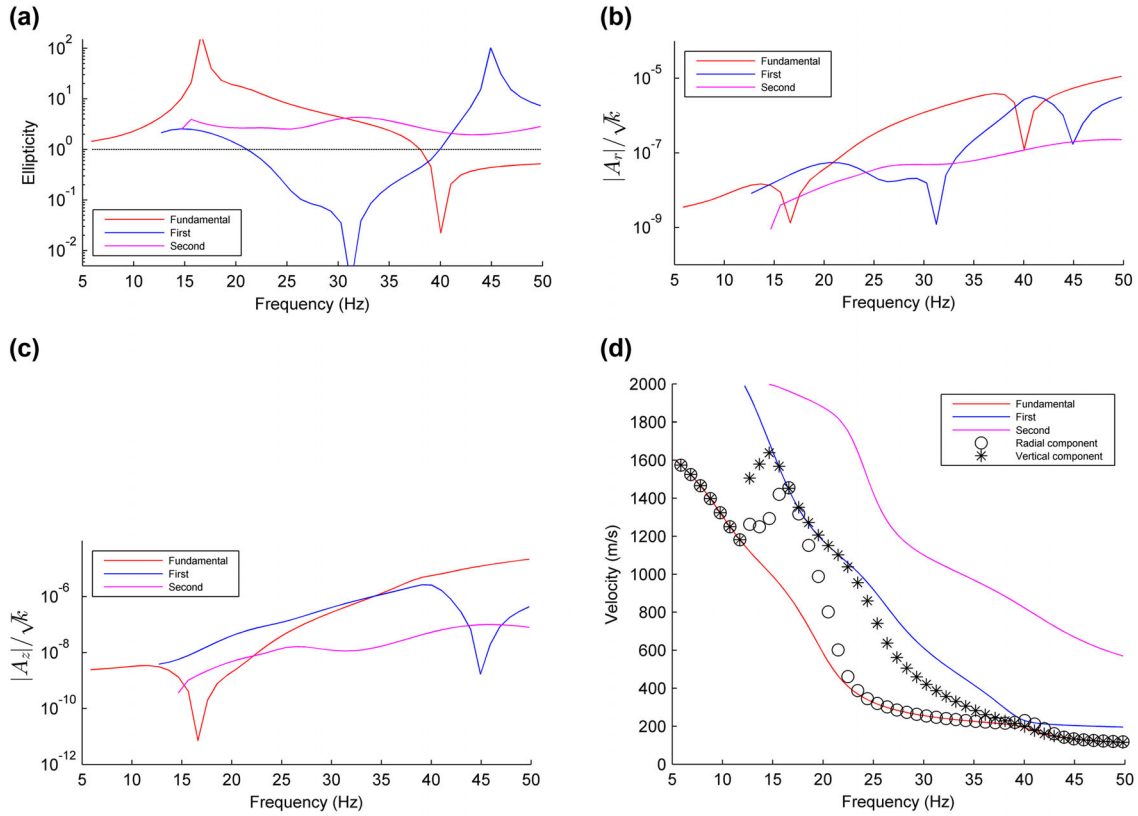

Figure 1 (a) Ellipticity, (b) radial amplitude response, (c) vertical amplitude response and (d) the apparent phase velocities of the Rayleigh waves in radial and vertical components for Model 1.

Table 2 Parameters of Model 2

Thickness (m)	V_p (m/s)	V_s (m/s)	Density (kg/m^3)
10	800	200	2000
Infinite	1200	600	2000

velocities of the fundamental mode and those of the first higher mode, since the fundamental mode and the first higher mode have comparative amplitude responses at those frequencies, as shown in Fig. 1(c).

Displacement differences between the radial and vertical components result in their diversity in the apparent phase velocity, so we can infer that the experimental dispersion curves picked from dispersion images may be different as well.

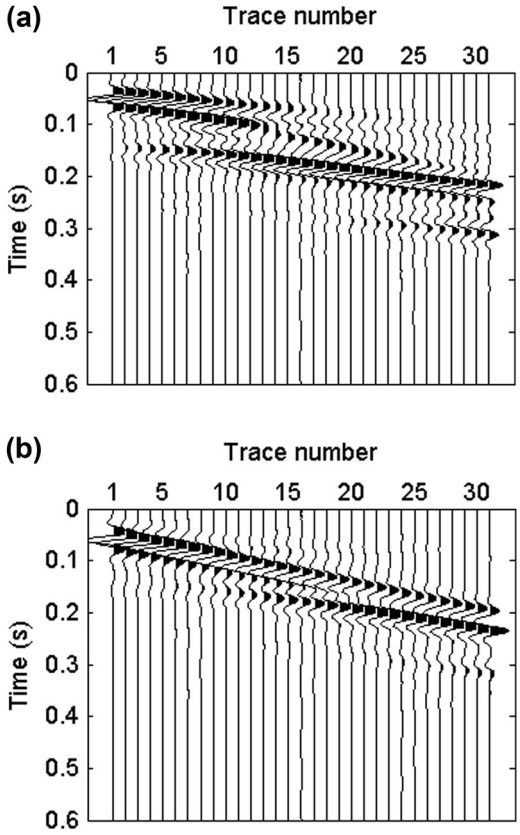

Figure 2 Synthetic data for Model 2: (a) the radial component and (b) the vertical component.

Table 3 Parameters of Model 3

Thickness (m)	V_p (m/s)	V_s (m/s)	Density (kg/m^3)
5	1000	300	2000
5	800	200	2000
Infinite	1200	600	2000

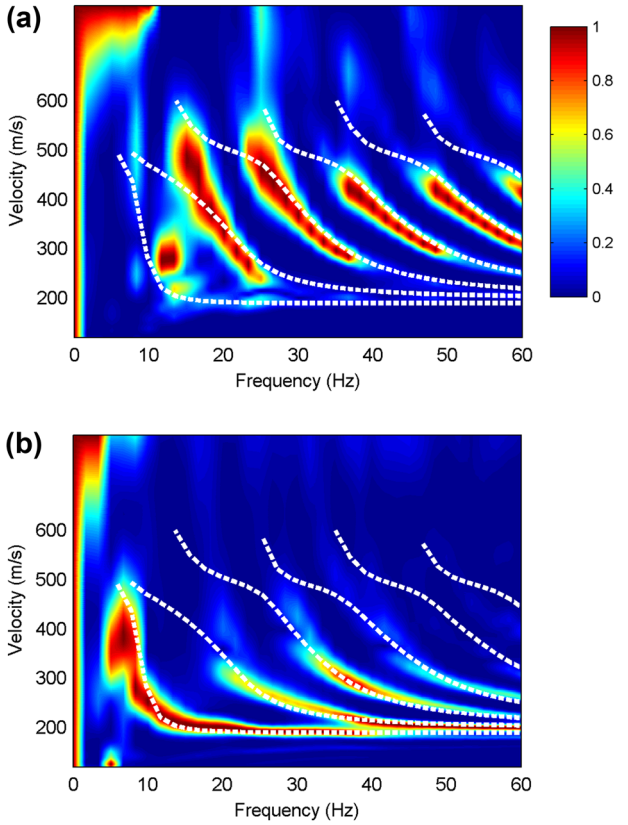

Figure 3 Dispersion images for Model 2 in the f–v domain: (a) the radial component and (b) the vertical component, where the white dashed lines are the theoretical dispersion curves.

Dispersive energy distributions for the radial and vertical components

A two-layer model (Model 2) is shown in Table 2. We simulate the wavefields using the staggered-grid finite-difference scheme with a vertical point source (a 20-Hz Ricker wavelet) at the surface. The size of spatial cell is 0.1 m × 0.1 m. The time step size is 0.1 ms. The order of accuracy of the scheme is 2 in the time domain and 12 in the spatial domain. The radial- and vertical-component seismic data are shown in Fig. 2. They are recorded on the surface with a 31-channel receiver array in line. The nearest offset is 2 m with a geophone interval of 1 m.

The dispersion images of the radial and vertical components are calculated by HLRT, as shown in Fig. 3, which is normalized at each frequency. Figure 3 also shows the theoretical dispersion curves of Rayleigh waves with the white

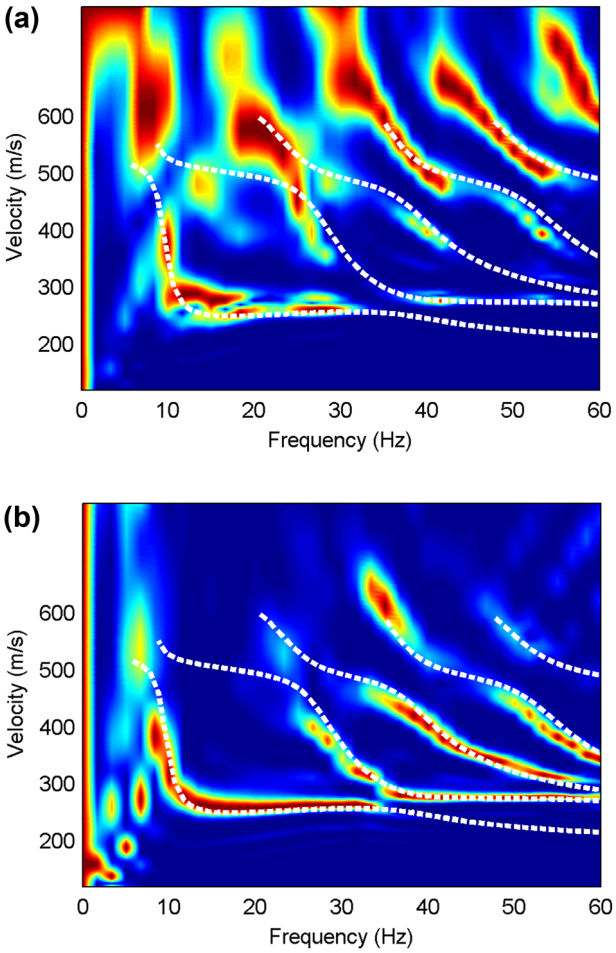

Figure 4 Dispersion images for Model 3 in the f–v domain: (a) the radial component and (b) the vertical component, where the white dashed lines are the theoretical dispersion curves.

dashed lines. We choose the spectral band of relative strong energy (over 0.7) as the effective spectral band. The fundamental mode is almost absent in the radial component but dominant in the vertical component. The higher modes in the radial component have much stronger energy than those in the vertical component. For any individual mode, the effective spectral band is different between the two components. For example, the spectral band of the second higher mode is 25–36 Hz for the radial component but 33–41 Hz for the vertical component.

A three-layer model with a soft layer (Model 3) is shown in Table 3. Dispersion images are shown in Fig. 4. The energy is distributed at different frequencies for the third higher mode between the two components. The first and second higher modes are distributed at relative high frequencies in the vertical component, but are distorted in the radial component. The fourth higher mode is absent in the vertical component but strong in the radial component. There exists much energy with velocities over the maximum S-wave velocity in both components, which is inferred to be caused by guided P-waves (Boiero, Wiarda and Vermeer 2013). Therefore, we can find there are different multi-mode dispersive energy distributions between the radial and vertical components. It may be beneficial for inversion to jointly use the two components.

METHODS

Conventional method: imaging dispersive energy of real-number seismic data

HLRT is traditionally used to image dispersive energy of the real-number Rayleigh waves. For the real-number

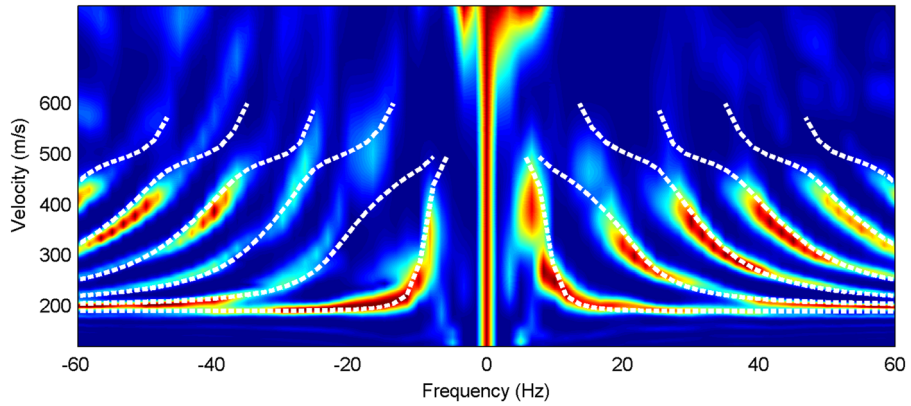

Figure 5 The dispersion image of the complex-vector data for Model 2 in the f–v domain, where the white dashed lines are the theoretical dispersion curves.

Table 4 Comparison of bandwidths among the radial, vertical and complex-vector data

Component	Fundamental mode (Hz)	First higher mode (Hz)	Second higher mode (Hz)	Third higher mode (Hz)	Fourth higher mode (Hz)
Radial	–	15–25	25–36	37–49	49–60
Vertical	6–39	30–60	33–41	–	–
Complex	7–31	19–29, 38–60	27–41	39–49	49–59

seismic data, the Radon coefficients at the positive frequencies are calculated in the frequency domain with formula (Luo *et al.* 2008, 2009):

$$\left(\lambda \mathbf{I} + \mathbf{W}_m^{-\mathrm{H}} \mathbf{L}^{\mathrm{H}} \mathbf{W}_d^{\mathrm{H}} \mathbf{W}_d \mathbf{L} \mathbf{W}_m^{-1}\right) \tilde{\boldsymbol{m}} = \mathbf{W}_m^{-\mathrm{H}} \mathbf{L}^{\mathrm{H}} \mathbf{W}_d^{\mathrm{H}} \mathbf{W}_d \boldsymbol{d}, \tag{7}$$

where $\tilde{\boldsymbol{m}} = \mathbf{W}_m \boldsymbol{m}$, $\mathbf{L}$ and $\mathbf{L}^{\mathrm{H}}$ are the operator matrices, λ is the regularization parameter, $\mathbf{I}$ is the identity matrix and $\boldsymbol{d}$ is the seismic data in the frequency-offset domain. $\boldsymbol{m}$ is the Radon coefficient in the frequency–velocity (f–v) domain. $\mathbf{W}_d$ is the data-weight matrix, and $\mathbf{W}_m$ is the model-weight matrix (Luo *et al.* 2008). The Radon coefficients at a negative frequency are conjugated to those at the corresponding positive frequency.

The dispersive energy E in f–v domain is obtained by the modulus operator and then normalized at each frequency (Xia, Xu and Miller 2007). Normalization can remove the influence of the source wavelet spectrum. For the frequency $f_0 \in (f_{\min}, f_{\max})$ and the velocity $v_0 \in (v_{\min}, v_{\max})$, the dispersive energy is

$$E(f_0, v_0) = \frac{|m(f_0, v_0)|}{\max\left(|m(f_0, v)|\right)}, \tag{8}$$

where $m(f_0, v)$ is a series of Radon coefficients at the frequency f_0 and all velocities. As inferred from equations (7) and (8), the dispersive energy at negative frequencies is equal to that at positive frequencies.

New method: imaging dispersive energy of complex-vector seismic data

First we construct a complex vector using the radial component as the real part and the vertical component as the imaginary part:

$$c(x, t) = r(x, t) + \mathrm{j} \cdot z(x, t), \tag{9}$$

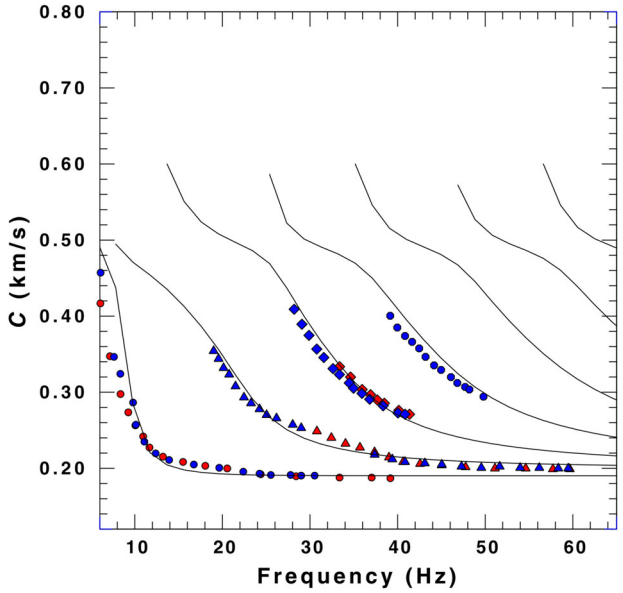

Figure 6 Comparison of dispersion curves extracted from the vertical (red point line) and complex-vector seismic data (blue point line). Different shapes of points correspond to the different modes and the black line is the theoretical dispersion curves.

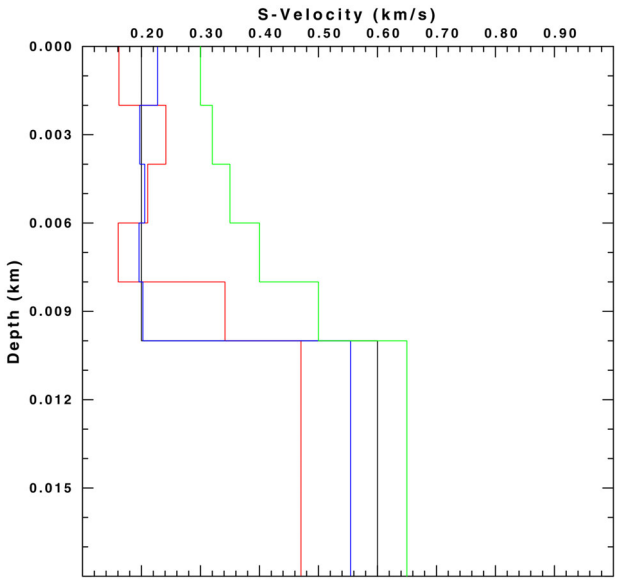

Figure 7 Comparison of the inverted S-wave velocity using the vertical (red line) and complex-vector seismic data (blue line). The black line is the theoretical S-wave velocity, and the green line is the initial S-wave velocity.

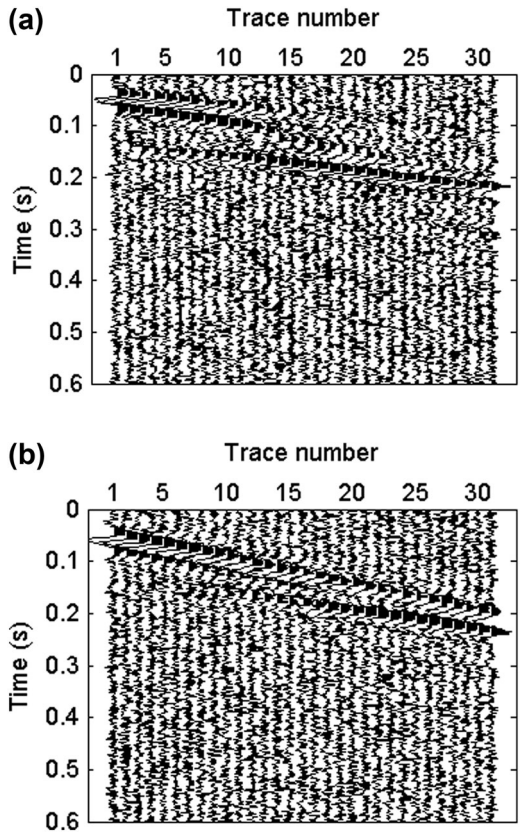

Figure 8 Noisy synthetic data: (a) the radial component and (b) the vertical component.

where $r(x, t)$ is the radial component, $z(x, t)$ is the vertical component and j is the imaginary unit.

Our study has found that the amplitude spectra of complex number seismic data at positive frequencies are unequal to those at the corresponding negative axis for elliptically polarized waves (Wang and Wang 2017). So we can infer that the Rayleigh-wave dispersive energy of complex-vector seismic data at the negative frequencies is not equal to that at the positive frequencies. For any individual mode, the dispersive energies either at the positive frequencies or at the corresponding negative frequencies can be important. The Radon coefficients of the complex-vector seismic data are also calculated using equation (7), but the input seismic data $\boldsymbol{d}$ are complex numbers via equation (9), and the symmetric assumption of the dispersion energy with frequency is not needed here. To avoid the influence of the source wavelet spectrum, we normalize the dispersive energy at a pair of frequencies $f = \pm f_0$ as follows:

$$E_c(f_0, v_0) = \frac{|m(f_0, v_0)|}{\max\left(|m(\pm f_0, v)|\right)}, \tag{10}$$

where $m(\pm f_0, v)$ is a series of Radon coefficients at a pair of frequencies $\pm f_0$ and all velocities.

SYNTHETIC EXAMPLES

Dispersion image of the complex-vector seismic data

With respect to the seismic data (Fig. 2), the dispersion image of the complex-vector seismic data is calculated, as shown in Fig. 5. It is obvious that the dispersive energy is not symmetrical about the zero frequency. The first, second and third higher modes are concentrated at the positive frequencies, while the fourth mode has more energy at the negative frequencies than at the positive frequencies. Statistically, the effective spectral bandwidths are different among the radial, vertical and complex-vector seismic data, as shown in Table 4. The comparison demonstrates that Rayleigh-wave dispersion based on the complex-vector seismic data has more modes, and the spectrum of Rayleigh waves shows as wider bands.

Effectiveness of dispersion curves extracted from the complex-vector seismic data

The dispersion curves are obtained by picking the phase velocities with the maxima energy from the dispersion images. We can find that more dispersion modes can be extracted from the complex-vector seismic data compared with the vertical component, although the fourth higher mode has a relatively great deviation from the theoretical dispersion curve, as shown in Fig. 6. In addition, the picked dispersion curves of the second and third higher modes have wider bandwidths than those when only the vertical component is used. All these characteristic will be beneficial to subsurface S-wave velocity estimation. As illustrated in Fig. 7, the S-wave velocity inverted by the complex-vector method is closer to the theoretical model than that by the vertical component. In our inversion of dispersion curves, the code 'surf96' (Herrmann and Ammon 2002) and the subdividing layering scheme (Shao and Li 2009) are employed.

Noisy synthetic data test

We add high-level white Gaussian noise to the seismic data (Fig. 2), as shown in Fig. 8. The signal-to-noise ratio (SNR) is 1. Figure 9 shows the dispersion images of the radial, vertical and complex-vector seismic data. The dispersive energy of the noisy data is discontinuous for the higher modes compared with noise-free data. In addition, the spectral bands are

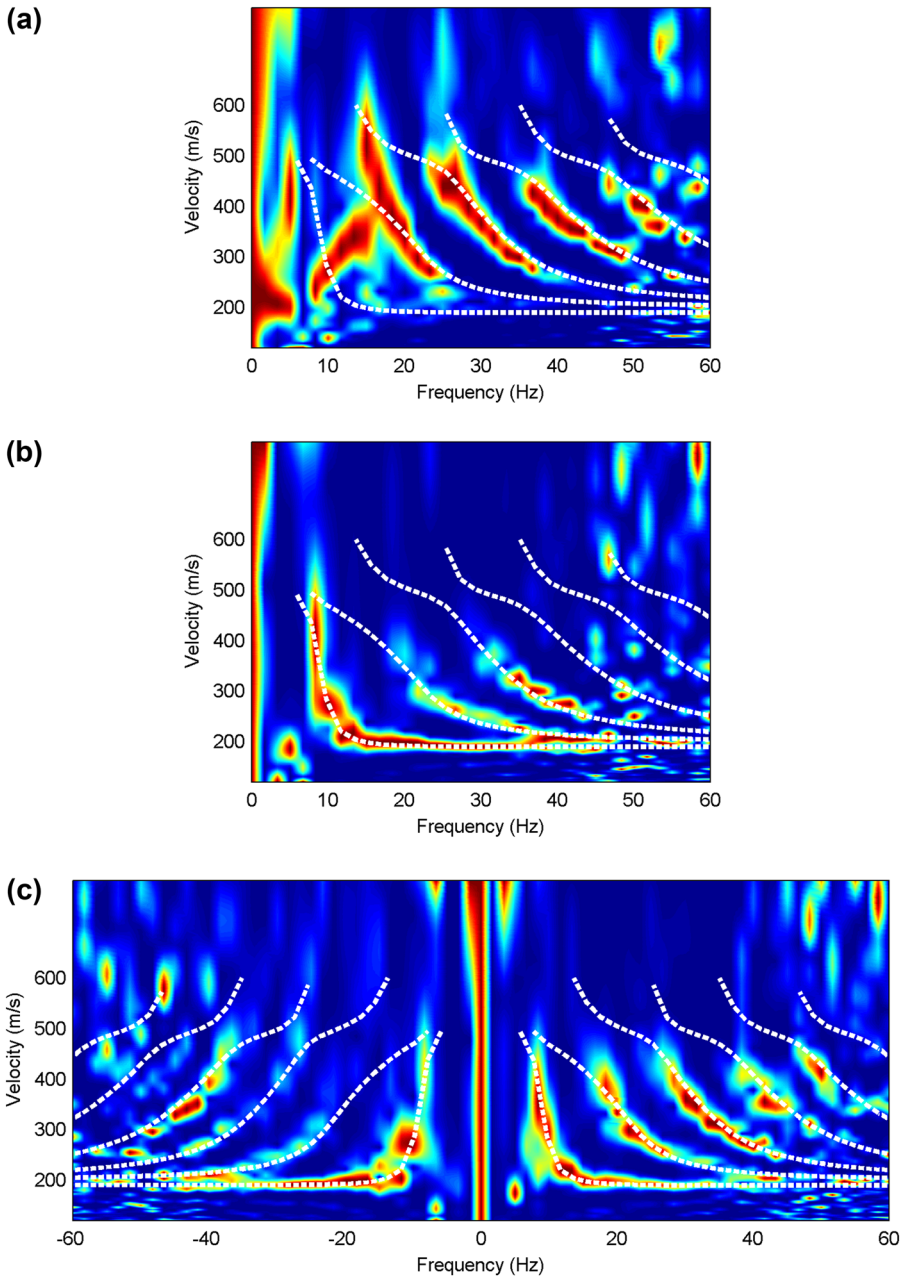

Figure 9 Dispersion images of noisy data in the f–v domain: (a) the radial component, (b) the vertical component and (c) the complex-vector seismic data, where the white dashed lines are the theoretical dispersion curves.

shorter. Mode jumping occurs at the frequency of 18 Hz in the radial component and at frequencies of 8 and 38 Hz in the vertical component. The vertical component is discontinuous for the first and second higher modes. The phase velocities are extracted from the vertical and complex-vector seismic data, as shown in Fig. 10. The phase velocities of the first higher mode at frequencies 8 and 38–44 Hz are misidentified with the fundamental mode in the vertical component. These phenomena will produce higher S-wave velocities than the theoretical model. As shown in Fig. 11, the inversion result using the vertical component shows a much greater velocity in the underlying layer, while the inversion result using the complex-vector seismic data is close to the theoretical S-wave velocities.

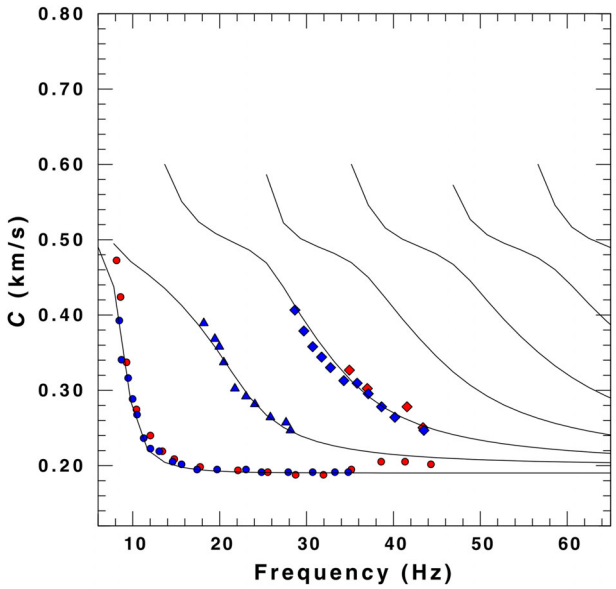

Figure 10 Comparison of dispersion curves extracted from the vertical (red point line) and complex-vector seismic data (blue point line) of noisy data. Different shapes of points correspond to the different modes. The black line is the theoretical dispersion curves.

FIELD EXAMPLE

The field data are acquired in Wanshousi, Beijing, China. They are activated by a hammer vertically impacting a fixture and recorded by a 15-channel in-line array with 4.5-Hz

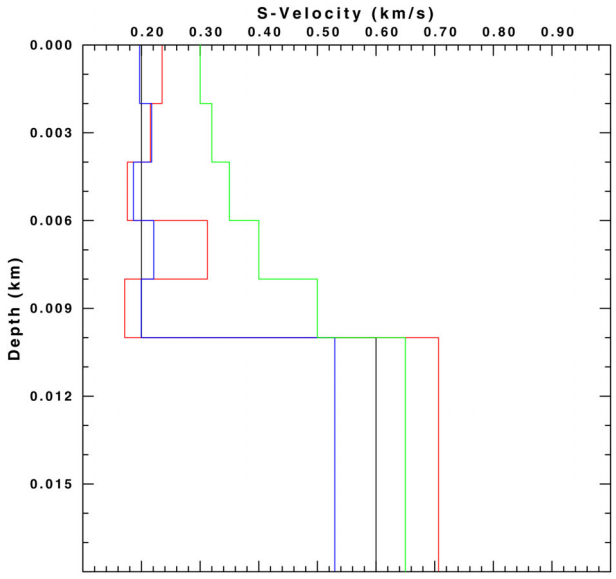

Figure 11 Comparison of the inversion result of noisy data using the vertical (red line) and complex-vector seismic data (blue line). The black line is the theoretical S-wave velocity. The green line is the initial S-wave velocity.

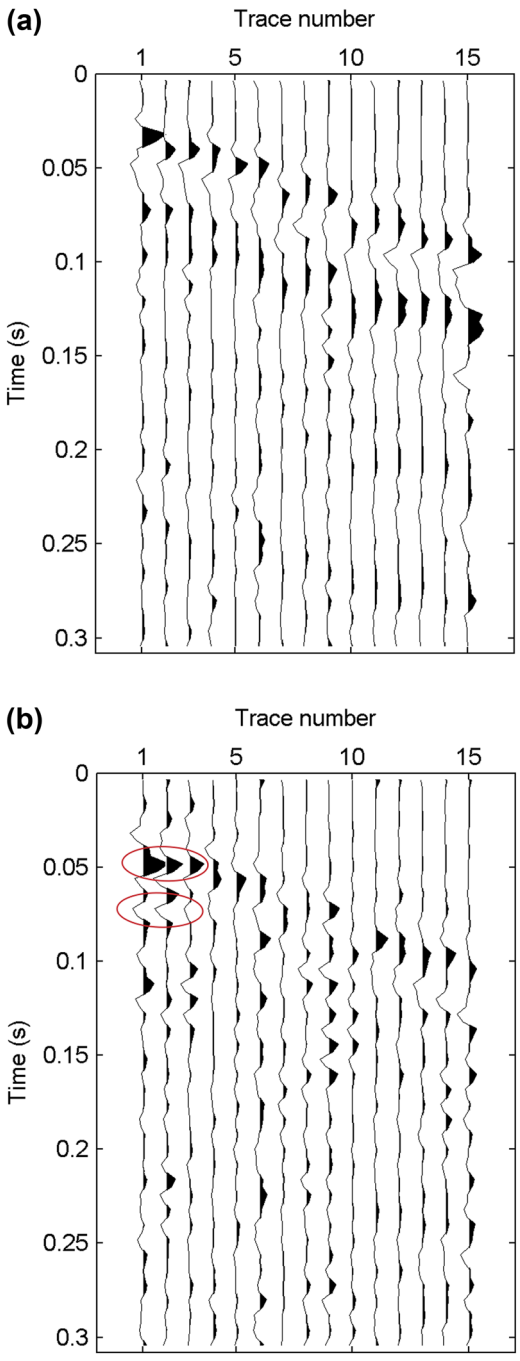

Figure 12 The field data: (a) the radial component and (b) the vertical component.

three-component (3C) geophones and a time sample interval of 4 ms. The nearest offset is 5 m with a geophone interval of 1 m. The radial and vertical components of the field data are shown in Fig. 12. The dispersion images of the radial, the vertical and the complex-vector seismic data are

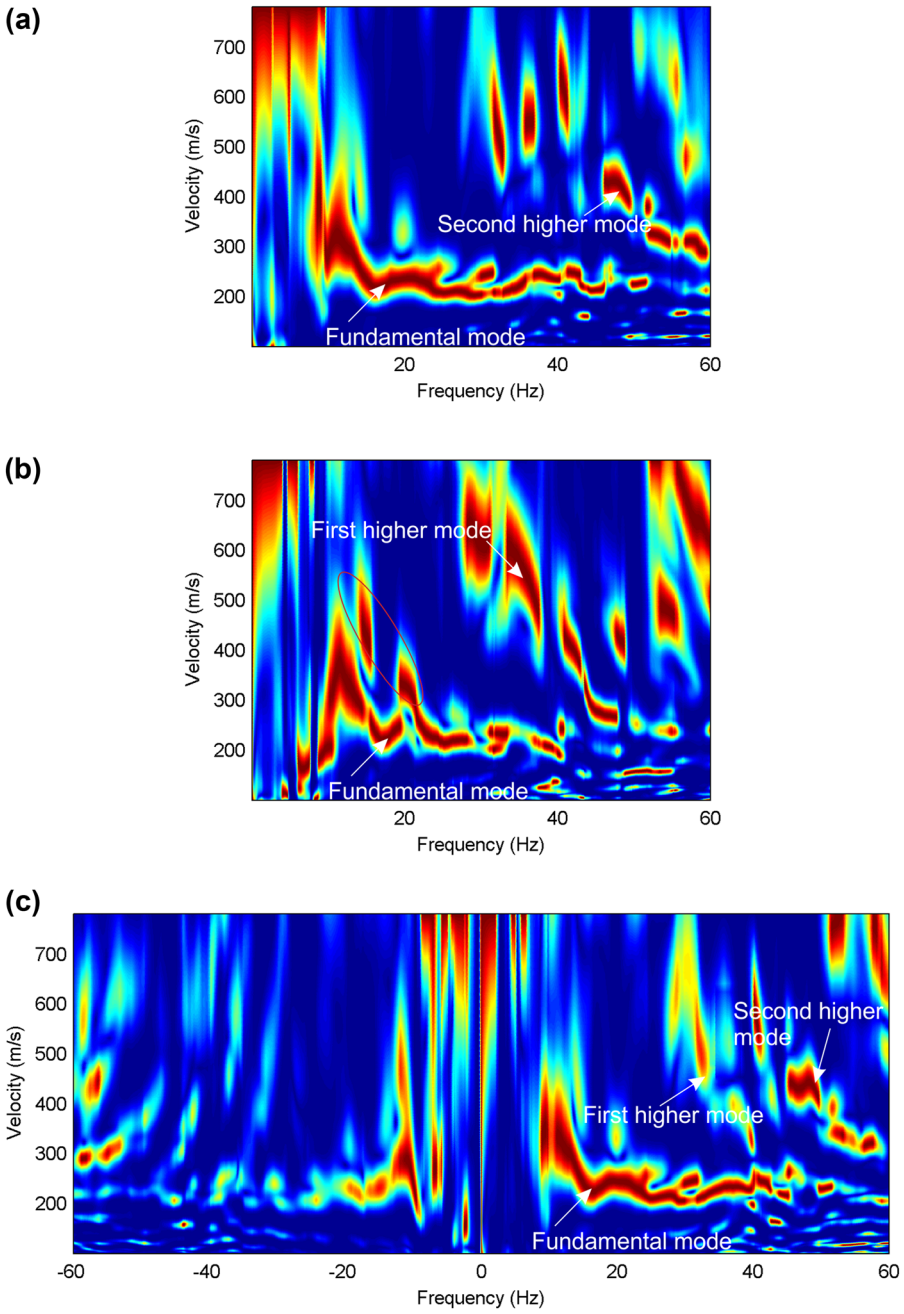

Figure 13 Dispersion images of field data in the f–v domain: (a) the radial component, (b) the vertical component and (c) the complex-vector seismic data.

shown in Fig. 13. Two key phenomena are observed from Fig. 13.

First, the fundamental mode is dominant in all components, but not all higher modes are existed in the dispersion images of real-number data (Fig. 13a,b). The first higher mode is strong in the vertical component, while the second higher mode is strong in the radial component. All of the modes can be identified from the complex-vector seismic data, and all of them are concentrated at the positive frequencies.

Second, the extra dispersive energy of the vertical component at frequencies 14–30 Hz, circled in Fig. 13(b), is vulnerable to being misidentified as a higher mode, because the extra energy is discontinuous with the dispersive energy of the fundamental mode. However, the phenomenon is not

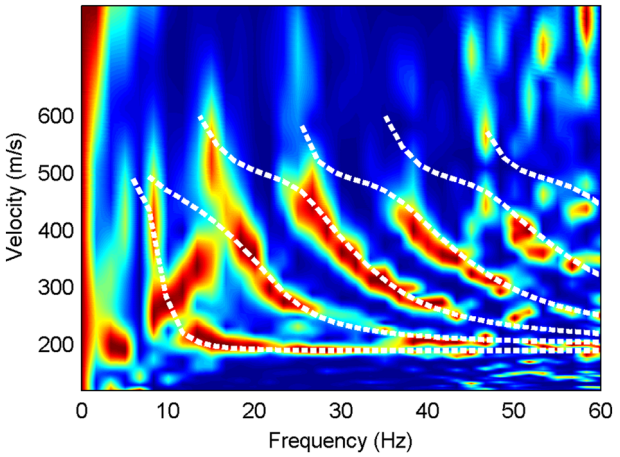

Figure 14 The stacked dispersion image corresponding to Fig. 9(a,b).

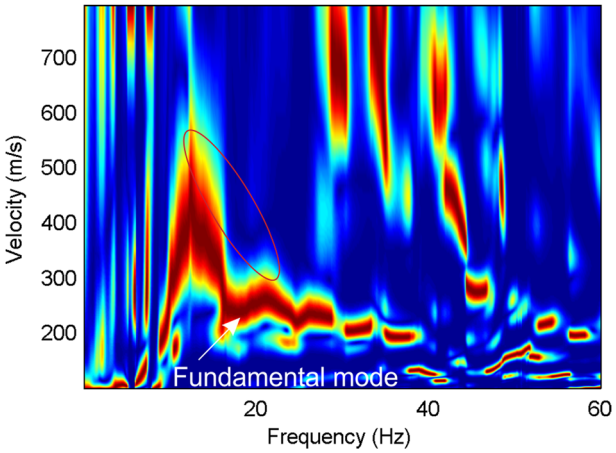

Figure 15 The dispersion image of the vertical-component field data when discarding the first three traces.

observed in the radial component or the complex-vector seismic data, so we believe that the mode misidentification would be overcome using complex-vector seismic data.

DISCUSSION

Our method for Rayleigh-wave dispersion analysis is based on complex-vector seismic data. Synthetic and field examples demonstrate that the dispersion image has more modes and wider spectral bands using our method than using the traditional vertical-component method. The polarization characteristics of Rayleigh waves make the dispersive energy concentrate on the one side of the whole f–v image, that is the side at positive or negative frequencies, while the energy of random noise or linearly polarized reflections is not the case. The Rayleigh waves are prominent against other interferences in the dispersion image, so the anti-noise test of our method can be explained.

To demonstrate the advantages of the complex-vector method further, the stacking method (Pan *et al.* 2018) for multicomponent Rayleigh waves is compared. The stacked image by the radial and vertical components is shown in Fig. 14. Compared with Fig. 9(c), we can find that the stacked image contaminates with strong interferences, so that wrong phase velocities are extracted. However, the problem is not existed using our complex-vector method.

The field example demonstrates that mode misidentification occurs using the vertical component, but it does not occur in radial and complex-vector seismic data. So it is not related to mode jumping. It may be caused by the near-field effects (e.g., Roy and Jakka 2017). As shown in Fig. 12(b), the circled seismic events in the first three traces of the vertical component have different slope from the radial component. To confirm the origin of the extra dispersive energy circled in Fig. 13(b), we discard the first three traces and image the residual traces. The extra energy is missing, as shown in Fig. 15. Therefore, near-field effects cause the high-velocity fake dispersive energy. However, the near-field effects are weak using our complex-vector method because of the concentration of Rayleigh-wave dispersive energy.

From Fig. 1(a), we observe that the ellipticity of the fundamental mode or the first higher mode is a function of frequency. It is known that ellipticity strongly depends on the velocity profile (Boaga *et al.* 2013; Knapmeyer-Endrun, Golombek and Ohrnberger 2017; Layadi, Semmane and Yelles-Chaouche 2018). The ellipticity-frequency curves of multi-mode Rayleigh waves are used to estimate the velocity structure (Knapmeyer-Endrun *et al.* 2017). When the ellipticity is included in inversion, the bedrock depth can be assessed better (Gouveia, Lopes and Gomes 2016). The method for multi-mode Rayleigh-wave ellipticity analysis will be studied in future research.

Furthermore, we conclude that mode jumping also occurs when the S-wave velocity increases with depth, as shown in Fig. 1(d). The mode jumping is caused by the relative values of the multi-mode displacement changing with frequency. From Fig. 1(d), we observe that the radial and vertical components "jump" from the fundamental mode to the first higher mode at frequencies of 14–16 Hz, because the first higher mode is absent before 13 Hz but has the greatest amplitude response among all modes at frequencies of 15–20 Hz (Fig. 1b,c). This is consistent with former conclusions (Lu *et al.* 2007).

CONCLUSIONS

We analyse different dispersion characteristics of the radial and vertical components, and propose a new method to jointly use both components. This study contributes to the understanding on multi-component Rayleigh waves. The proposed method is based on complex-vector algebra, which can provide more accurate and reliable phase velocity dispersion curves than the traditional vertical-component method. Synthetic and field examples demonstrate the following:

1. Multi-mode Rayleigh waves have different apparent phase velocities between the radial and the vertical components, which is caused by different amplitude responses of the two components;

2. The radial and the vertical components are complementary to each other in the terms of dispersion information. Since more modes and wider spectral bands of Rayleigh waves can be utilized, it can be expected that a more accurate structure for subsurface S-wave velocity field could be obtained by using them jointly; and

3. The proposed method can weaken near-field effects and obtain a reliable dispersion image without mode misidentification. Because of the concentration of Rayleigh-wave dispersive energy, the method has stronger anti-noise performance.

ACKNOWLEDGEMENTS

We thank Lixia Sun for simulating Rayleigh waves and Aimin Xue (Beijing Petrosound Geoservices Stock Corp) for providing the field data. We greatly acknowledge financial support by the National Natural Science Foundation of China (U1839208, 41425017, 41874166), the National Science and Technology Major Project (2017ZX05018005) and the National Key R&D Program of China (2016YFC0600301).

REFERENCES

Aki K. and Richards P.G. 2002. *Quantitative Seismology*. University Science Books.

Boaga J., Cassiani G., Strobbia C.L. and Vignoli G. 2013. Mode misidentification in Rayleigh waves: ellipticity as a cause and a cure. *Geophysics* **78**, 17–28.

Boiero D., Wiarda E. and Vermeer P. 2013. Surface-and guided-wave inversion for near-surface modeling in land and shallow marine seismic data. *The Leading Edge* **32**, 638–646.

Dal Moro G. 2014. *Surface Wave Analysis for Near Surface Applications*. Elsevier.

Dal Moro G. and Ferigo F. 2011. Joint analysis of Rayleigh-and love-wave dispersion: issues, criteria and improvements. *Journal of Applied Geophysics* **75**, 573–589.

Dal Moro G., Moura R.M.M. and Moustafa S.S. 2015. Multi-component joint analysis of surface waves. *Journal of Applied Geophysics* **119**, 128–138.

Dal Moro G., Moustafa S.S. and Al-Arifi N.S. 2018. Improved holistic analysis of Rayleigh waves for single-and multi-offset data: joint inversion of Rayleigh-wave particle motion and vertical-and radial-component velocity spectra. *Pure and Applied Geophysics* **175**, 67–88.

Gouveia F., Lopes I. and Gomes R.C. 2016. Deeper vs profile from joint analysis of Rayleigh wave data. *Engineering Geology* **202**, 85–98.

Harkrider D.G. 1970. Surface waves in multilayered elastic media. Part II. Higher mode spectra and spectral ratios from point sources in plane layered earth models. *Bulletin of the Seismological Society of America* **60**, 1937–1987.

Harmon N., Forsyth D. and Webb S. 2007. Using ambient seismic noise to determine short-period phase velocities and shallow shear velocities in young oceanic lithosphere. *Bulletin of the Seismological Society of America* **97**, 2009–2023.

Haskell N.A. 1953. The dispersion of surface waves on multilayered media. *Bulletin of the Seismological Society of America* **43**, 17–34.

Herrmann R. and Ammon C. 2002. *Computer Programs in Seismology*, version 3.30. St. Louis University, St. Louis, MO.

Ikeda T. and Matsuoka T. 2013. Computation of Rayleigh waves on transversely isotropic media by the reduced delta matrix method. *Bulletin of the Seismological Society of America* **103**, 2083–2093.

Ikeda T., Matsuoka T., Tsuji T. and Nakayama T. 2015. Characteristics of the horizontal component of Rayleigh waves in multimode analysis of surface waves. *Geophysics* **80**, 1–11.

Ivanov J., Miller R.D., Xia J. and Peterie S. 2010. Multi-mode inversion of multi-channel analysis of surface waves (MASW) dispersion curves and high-resolution linear radon transform (HRLRT). SEG Technical Program Expanded Abstracts 2010, 1902–1907. Society of Exploration Geophysicists.

Knapmeyer-Endrun B., Golombek M.P. and Ohrnberger M. 2017. Rayleigh wave ellipticity modeling and inversion for shallow structure at the proposed insight landing site in Elysium Planitia, Mars. *Space Science Reviews* **211**, 339–382.

Lai C.G., Mangriotis M.D. and Rix G.J. 2014. An explicit relation for the apparent phase velocity of Rayleigh waves in a vertically heterogeneous elastic half-space. *Geophysical Journal International* **199**, 673–687.

Layadi K., Semmane F. and Yelles-Chaouche A. 2018. S-wave velocity structure of Chlef City, Algeria, by inversion of Rayleigh wave ellipticity. *Near Surface Geophysics* **16**, 328–339.

Lu L., Wang C. and Zhang B. 2007. Inversion of multimode Rayleigh waves in the presence of a low-velocity layer: numerical and laboratory study. *Geophysical Journal International* **168**, 1235–1246.

Luo Y., Xia J., Miller R.D., Xu Y., Liu J. and Liu Q. 2008. Rayleigh-wave dispersive energy imaging using a high-resolution linear radon transform. *Pure and Applied Geophysics* **165**, 903–922.

Luo Y., Xia J., Miller R.D., Xu Y., Liu J. and Liu Q. 2009. Rayleigh-wave mode separation by high-resolution linear radon transform. *Geophysical Journal International* **179**, 254–264.

Mi B., Xia J., Shen C. and Wang L. 2018. Dispersion energy analysis of Rayleigh and Lovewaves in the presence of low-velocity layers in near-surface seismic surveys. *Surveys in Geophysics* **39**, 271–288.

Olafsdottir E.A., Bessason B. and Erlingsson S. 2018. Combination of dispersion curves from masw measurements. *Soil Dynamics and Earthquake Engineering* **113**, 473–487.

Pan Y., Schaneng S., Steinweg T. and Bohlen T. 2018. Estimating S-wave velocities from 3D 9-component shallow seismic data using local Rayleigh-wave dispersion curves—a field study. *Journal of Applied Geophysics* **159**, 532–539.

Roy N. and Jakka R.S. 2017. Near-field effects on site characterization using MASW technique. *Soil Dynamics and Earthquake Engineering* **97**, 289–303.

Shao G. and Li Q. 2009. Subdividing layering method in dispersion curves inversion of surface wave, 2009 International Geophysical Conference and Exposition, April 24–27, 2009. Beijing, China, pp. 234–234.

Song X., Gu H., Liu J. and Zhang X. 2007. Estimation of shallow subsurface shear-wave velocity by inverting fundamental and higher-mode Rayleigh waves. *Soil Dynamics and Earthquake Engineering* **27**, 599–607.

Tokimatsu K., Tamura S. and Kojima H. 1992. Effects of multiple modes on Rayleigh wave dispersion characteristics. *Journal of Geotechnical Engineering* **118**, 1529–1543.

Vaziri Astaneh A. and Guddati M.N. 2016. Improved inversion algorithms for near-surface characterization. *Geophysical Journal International* **206**, 1410–1423.

Wang C. and Wang Y. 2017. Ground roll attenuation using polarization analysis in the TFK domain. *Geophysical Journal International* **210**, 240–254.

Xia J., Miller R.D. and Park C.B. 1999. Estimation of near-surface shear-wave velocity by inversion of Rayleigh waves. *Geophysics* **64**, 691–700.

Xia J., Miller R.D., Park C.B. and Tian G. 2003. Inversion of high frequency surface waves with fundamental and higher modes. *Journal of Applied Geophysics* **52**, 45–57.

Xia J., Xu Y., Luo Y., Miller R.D., Cakir R. and Zeng C. 2012. Advantages of using multichannel analysis of Love waves (MALW) to estimate near-surface shear-wave velocity. *Surveys in Geophysics* **33**, 841–860.

Xia J., Xu Y. and Miller R.D. 2007. Generating an image of dispersive energy by frequency decomposition and slant stacking. *Pure and Applied Geophysics* **164**, 941–956.

Yao H., Gouedard P., Collins J.A., McGuire J.J. and van der Hilst R.D. 2011. Structure of young east pacific rise lithosphere from ambient noise correlation analysis of fundamental-and higher-mode Scholte-Rayleigh waves. *Comptes Rendus Geoscience* **343**, 571–583.

Zhang S.X. and Chan L.S. 2003. Possible effects of misidentified mode number on Rayleigh wave inversion. *Journal of Applied Geophysics* **53**, 17–29.

APPENDIX

For the displacement-stress vector $S = [\,\frac{u_x}{c}\ \frac{u_z}{c}\ \sigma_{xz}\ \sigma_{zz}\,]$, Harkrider (1970) proposed a matrix to analyse surface waves in layered elastic media:

$$\mathbf{R} = \mathbf{T}_n^{-1}(\mathbf{A}_{n-1}\mathbf{A}_{n-2}\ldots\mathbf{A}_1), \tag{A1}$$

where $\mathbf{A}_i (i = 1, 2, \ldots, n-1)$ is the Thomson–Haskell layered matrix of the ith layer (1953).

$$\mathbf{T}_n^{-1} = \begin{bmatrix} i\gamma_n r^*_{\alpha n} & \gamma_n - 1 & -\frac{i r^*_{\alpha n}}{\rho_n c^2} & \frac{1}{\rho_n c^2} \\ 1-\gamma_n & i\gamma_n r^*_{\beta n} & \frac{1}{\rho_n c^2} & \frac{i r^*_{\beta n}}{\rho_n c^2} \\ i\gamma_n r^*_{\alpha n} & 1-\gamma_n & -\frac{i r^*_{\alpha n}}{\rho_n c^2} & \frac{1}{\rho_n c^2} \\ \gamma_n - 1 & i\gamma_n r^*_{\beta n} & -\frac{1}{\rho_n c^2} & \frac{i r^*_{\beta n}}{\rho_n c^2} \end{bmatrix}, \tag{A2}$$

where ρ_n is the density of the nth layer, $\gamma_n = 2(\beta_n/c)^2$ and β_n is the S-wave velocity. $r^*_{\alpha n}$ and $r^*_{\beta n}$ are the conjugations of $r_{\alpha n}$ and $r_{\beta n}$, which are given by Haskell (1953).